Research Article | Vol. 34, No. 8 / 20 Apr 2026 / Optics Express 15713

Optics EXPRESS

Laser-based manufacturing of fused silica optics: figure error correction using laser beam figuring

EMRAH ULUZ,[1,2,†,*] SHENGYI DAI,[2,†] EDGAR WILLENBORG,[1] AND CONSTANTIN HAEFNER[2]

[1] *Fraunhofer Institute for Laser Technology ILT, Steinbachstr. 15, 52074 Aachen, Germany*
[2] *Chair for Laser Technology LLT, RWTH Aachen University, Templergraben 55, 52062 Aachen, Germany*
[†] These authors contributed equally.
[*] *emrah.uluz@ilt.fraunhofer.de*

Abstract: Demand for complex, application-specific optics requires processes that deliver high surface quality and figure accuracy at reduced cost and lead time. This work investigates laser beam figuring (LBF) as a deterministic, laser-based step in an integrated manufacturing chain for fused silica optics. LBF uses spatially selective CO_2-laser irradiation to remove material in the nanometer range according to the difference between the actual and target surface geometry. Pulse-duration modulation enables precise depth control while maintaining low surface roughness. Building on previous studies, we address two critical gaps in the state-of-the-art. First, we experimentally determine the long-term stability of laser-induced densified regions over an unprecedented 80-week observation period, demonstrating statistically robust process stability essential for industrial applications. Second, we systematically map the transition from densification-dominated regimes (< 10 nm) to true ablation, identifying optimal process windows (dx = 10 µm, dy = 30 µm) that enable reproducible nanometer-scale figure correction with area rates competitive to conventional methods. Figure error correction experiments demonstrate RMS reduction from 79.2 nm to 30.6 nm in a single pass. However, LBF introduces high-frequency surface features (λ < 100 µm), suggesting integration with chemo-mechanical post-polishing for applications requiring ultra-smooth surfaces. The results provide a quantitative foundation for LBF as a complementary technology to ion beam figuring and magnetorheological finishing, particularly suited for rapid prototyping and laser-based process chains.

Published by Optica Publishing Group under the terms of the Creative Commons Attribution 4.0 License. Further distribution of this work must maintain attribution to the author(s) and the published article's title, journal citation, and DOI.

1. Introduction

1.1. Manufacturing processes for optical elements

Manufacturing processes for optical components are classified into the main groups of primary shaping, forming, material removal, joining, coating, and altering material properties [1–5]. For glass optics, two primary manufacturing routes exist which are called forming and material removal.

Precision glass molding, a forming process, is a cost-effective method for the mass production of complex optical elements, including aspheres. However, its inherent limitations in achievable surface finish and form accuracy necessitate subsequent finishing steps for high-end applications [6]. The alternative route is material removal, a sequence of subtractive processes. Initial shaping is typically performed by grinding, which utilizes a tool with bonded diamond abrasives with grain sizes approx. 2–400 µm to establish the basic geometry. A critical consequence of grinding brittle materials like glass is the induction of subsurface damage [6]. This damaged layer must be removed through finer abrasive techniques. Lapping employs a loose abrasive to remove the bulk

#591743 https://doi.org/10.1364/OE.591743
Journal © 2026 Received 28 Jan 2026; revised 13 Mar 2026; accepted 30 Mar 2026; published 17 Apr 2026

of the subsurface damage and improve form accuracy. The final optical-grade surface is achieved through polishing, a chemo-mechanical process where a slurry and pad interact to produce a smooth surface with minimal roughness [6].

The selection between these routes is primarily economic: precision molding is favored for high-volume production due to low per-unit costs, whereas subtractive processes are more viable for low-to-medium volumes as they avoid the high initial cost and lead time of mold fabrication [7,8]. To meet the most stringent specifications for surface form error, conventional polishing is often insufficient. Advanced, deterministic finishing processes are required to correct residual form errors and mid-to-high spatial frequency waviness. These technologies include Fluid Jet Polishing (FJP) [9,10], Plasma Jet Machining (PJM) [11,12], Magneto-Rheological Finishing (MRF) and the related bonnet polishing process [13–16], and Ion Beam Figuring (IBF) [17–19].

MRF is a finishing process that uses suspension of magnetic particles in place of a conventional polishing tool. When a magnetic field is applied, the particles become polarized and form solidified chains along the field lines, the stiffness of which can be altered by varying the field strength. The surface to be processed is moved over this suspension and pressed slightly into the fluid. Material removal is achieved by the motion of a disc or wheel and the abrasive medium within the viscous suspension. The amount of locally removed material is governed by the dwell time of the workpiece, whose movement is typically computer-controlled. In conjunction with measurement data, the actual surface of the optics is corrected to match the target surface. The MRF process does not induce damage to the processed surfaces. MRF enables the nano-finishing of convex surfaces with small radii of curvature, achieving a surface roughness of Ra = 2.4 nm [15] and below. However, the dimensions of the carrier wheels impose limitations on the processing of concave and complex surfaces. Typical processing times for precision MRF polishing of fused silica aspheres range from 20 min to several hours, depending on the size of the area being corrected. The size of the carrier wheel also limits the spatial resolution of MRF to surface wavelengths of approximately $\lambda_O > 3000\,\mu m$ [13–15].

Another method for surface figuring optical elements, particularly aspherical lenses, is Ion Beam Figuring. IBF is based on particle collisions at the atomic level, where the structural and chemical properties of solid materials are intentionally altered by high-energy ion bombardment. This process is typically conducted in a vacuum chamber and removes material from the surface region on a scale of a few nanometers. The longer the dwell time of the ion beam at a specific location, the greater the local material removal. The primary advantage of IBF over conventional polishing methods is its non-contact nature. IBF is well-suited for the final finishing and figuring of optical elements that demand extremely high surface quality with corrected mid- and high-spatial frequency errors, such as those used in Extreme Ultraviolet (EUV) lithography and soft X-ray optics [18]. Using IBF, a root mean square roughness of less than 0.2 nm can be achieved. A disadvantage, however, is that this process is limited to niche optics, materials, and specifications for various reasons. Due to the complex equipment and the low removal depth per cycle compared to mechanical polishing methods, IBF is cost-intensive and difficult to implement for large optical elements [17–19].

1.2. Laser-based manufacturing of optical elements

The increasing complexity of optical systems demands geometrically sophisticated optical elements, posing significant challenges to established manufacturing processes. Laser-based machining technologies offer substantial advantages over conventional mechanical processes through non-contact processing, high flexibility, and reduced processing times. Precise control of laser parameters enables both the fabrication of complex surface geometries and highly automated process control with reduced manufacturing costs. Pioneering work on laser-based manufacturing of fused silica optical elements was conducted by Nowak et al. [20,21]. Using acousto-optically modulated CO_2 laser radiation, they achieved controlled material removal up to

$30 \pm 0.15\,\mu m$ depth with crack-free processing. Removal rates correlate directly with radiation intensity, pulse duration, and spot size. Besides shape manufacturing Nowak demonstrated pulsed laser polishing of the ablated surfaces with polishing rates up to $0.27\,cm^2/s$, where the area rate denotes the processed surface area per unit time [20]. Parallel developments by Hecht [22] and Richmann [23] established continuous CO_2 laser polishing processes for fused silica, based on Temple et al. [24]. This technique reduced surface roughness from 200 - 800 nm to 5 - 15 nm at area rates of $0.21\,cm^2/s$ [25]. Building on these foundations, Fraunhofer ILT developed an integrated laser-based process chain for spherical, aspherical, and freeform optical elements in 2011 [26]. This three-stage process chain comprises shape generation through laser-induced ablation, surface polishing, and figure error correction.

Form generation utilizes either CO_2 laser radiation or ultrashort pulses. USP lasers offer higher lateral resolution (0.1 - 0.5 µm vs. 10 - 40 µm) and material versatility but cause higher costs and microcrack formation [2]. Selective Laser-induced Etching (SLE) combines laser-induced structural modification with wet chemical etching (KOH/HF), achieving up to 10.000-fold increased etch rates [27,28].

Laser polishing employs 2D galvanometer scanners for oscillating beam deflection, achieving homogeneous energy distribution along one line [29]. Surface temperature reaches the softening range below vaporization temperature, enabling surface tension-driven redistribution of the glass resulting in improved surface quality [22,25]. Spectral roughness analyses show comparable or lower Sa values compared to conventional polishing for spatial wavelengths $\lambda < 100\,\mu m$ [3,30]. For $\lambda > 100\,\mu m$, Sa values increase, requiring subsequent figure error correction.

1.3. Laser-based figure error correction using laser beam figuring

Local figure correction of fused silica surfaces can be performed using Laser Beam Figuring (LBF), a process where laser radiation is employed for the site-selective, nanometer-scale removal of material from a surface. Initial investigations into the nanoscale laser-based material removal from fused silica were conducted by Nowak et al. in 2003 [21]. This early work on single-pulse ablation was followed by further studies from Wlodarczyk [31], Robin et al. [32], and Elhadj et al. [33]. A common element in these experiments was the use of a CO_2 laser source, with variations in beam diameter and laser power depending on the focusing optics employed.

Heidrich et al. were the first to investigate the LBF process specifically for the deterministic figure correction of fused silica surfaces [2,26,34]. Their work compared the effects of CO_2 laser radiation with that of USP lasers. It was demonstrated that USP laser processing had a minimum achievable removal depth of 210 nm, rendering it unsuitable for the correction of surface form errors in the low single- to double-digit nanometer range. While early investigations using conventional ultrashort pulse lasers reported subsurface damage including micro-cracks [2,26,34], recent advances in GHz-burst mode femtosecond processing have demonstrated improved surface quality [35]. However, the CO_2-based LBF approach investigated in this work offers distinct and complementary advantages. First, it enables full-aperture figure error correction over areas exceeding $16 \times 16\,mm^2$, in contrast to the localized polishing demonstrated in [35]. Second, it can be seamlessly integrated into a laser-based process chain spanning ablation, laser polishing, and LBF without requiring tool changes. Third, the approach demonstrates quantified long-term stability over 80 weeks, which is critical for applications with stringent environmental specifications and has not been demonstrated for fs-processed surfaces. Fourth, it provides precise control over densification-dominated regimes with less than 10 nm removal for ultra-fine corrections. Finally, CO_2 lasers offer significantly lower capital and operational costs, being 10 - 20x more economical than femtosecond systems. These factors position CO_2-LBF as a complementary, rather than competing, technology particularly suited for rapid prototyping and industrial-scale manufacturing.

Optics EXPRESS

Complementary research using femtosecond laser processing has explored alternative approaches to fused silica surface modification. Qiao et.al [35] investigated GHz-burst mode femtosecond laser polishing, demonstrating roughness reduction on small areas ($6 \times 6\,\mu m^2$ evaluation regions) of pre-polished substrates. While these fs-laser techniques achieve high lateral resolution ($< 1\,\mu m$), they differ fundamentally from the present work in scope in that fs-polishing targets local surface smoothing on already polished optics, whereas the CO_2-LBF process addresses full-aperture figure error correction with removal depths from sub-nm to 45 nm across cm^2-scale areas.

Investigations by Weingarten [3] employed modulated CO_2 laser radiation for both single-pulse and area-wide removal. The studies showed that the fused silica surface could be densified and ablated over a wide area. However, the laser source used did not permit the precise control over the removal depth that is a critical prerequisite for the fabrication of high-end optics. Building upon the previous findings, Uluz [30] investigated the removal behaviour and reproducibility of the LBF process using a power-stabilized CO_2 laser source. Following a thermal annealing cycle applied to a fused silica sample (using parameters $P_L = 25$ W, $t_p = 45\,\mu s$, and $d_S = 246\,\mu m$), the surface topography was analyzed. The measurements yielded a mean surface deviation of $z_{ab} = 0.73$ nm with a corresponding standard deviation of $\pm\,0.45$ nm. The original study [30] noted that the resulting large relative uncertainty (61.6%) was attributed to the 1 nm resolution limit of the measurement instrument. However, a rigorous interpretation of this finding must account for this instrumental limitation. Given that the calculated mean value of 0.73 nm is smaller than the instrument's specified resolution limit (1 nm), the reported value falls below the threshold of detectable change. Therefore, these data do not provide statistically significant evidence of a net, area-wide material removal. The measured fluctuations are consistent with the instrument's measurement uncertainty and noise floor when operating at its detection limit. A summary of experimental investigations into the nm-scale laser ablation of fused silica is presented in Table 1.

Table 1. Overview of experimental investigations into laser-based nanometer ablation.

Author, Year	Nowak, 2003	Wlodarczyk, 2011	Robin, 2012	Elhadj, 2012	Heidrich, 2014		Weingarten, 2017	Uluz, 2021	Qiao, 2025
Laser mode	modulated			cw	cw	pulsed	modulated		GHzBurst
Laser source	CO_2-Laser					USP	CO_2-Laser		USP
P_L in W	N/A	17	4.5	6.5-7.2	16	35	25	25	40
t_p in us	50	10	$250 \cdot 10^3$	$5 \cdot 10^6$	230	$1 \cdot 10^{-6}$	80	45	$2 \cdot 10^{-7}$
d_L in µm	47	47	700	1000	250	50	300	246	6.2
Removal	single-shot	line	single-shot	single-shot	area	single-shot	area	area	area
z_{ab} in nm	200	7	30	100	6.3	210	3	0.73	10
$\Delta z_{ab}/z_{ab}$ in %	25	N/A	N/A	N/A	34.9	N/A	11.4	61.6	N/A

While the studies established the fundamental feasibility of laser-based nanoscale material removal, several critical aspects remain insufficiently characterized for industrial deployment. Most notably, the long-term stability of laser-induced surface modifications prerequisite for optical applications with stringent environmental specifications has not been rigorously quantified beyond short observation periods. Additionally, the interplay between process parameters (pulse duration, spatial overlap) and the resulting surface quality across different removal regimes requires systematic mapping to define reproducible process windows. Finally, comparative benchmarking against established deterministic finishing technologies (MRF, IBF) is needed to position LBF within the broader manufacturing landscape.

Optics EXPRESS

This work directly addresses these deficits through three key contributions. First, an 80-week metrological study quantifying the temporal stability of densified surfaces using a hierarchical statistical model (Linear Mixed Model, LMM) that explicitly accounts for spatial process inhomogeneity, demonstrating no statistically significant relaxation within the observation window. Second, comprehensive parameter mapping to identify the transition from densification to ablation-dominated regimes, establishing optimal operating points that balance removal efficiency with surface quality. Third, experimental demonstration of figure error correction on laser-polished substrates, revealing both the process capability (RMS reduction from 79.2 nm to 30.6 nm) and inherent limitations. These results provide a quantitative basis for integrating LBF into laser-based manufacturing chains for high-precision fused silica optics.

2. Materials and methods

2.1. Experimental setup

The experimental setup, based on the work of Weingarten [3], and Uluz [30], employs a power-stabilized CO_2 laser source. An acousto-optic modulator (AOM) is used to modulate the laser pulses. The pulses are subsequently guided over a beam path of $\approx$ 10 m via highly reflective mirrors. Figure 1 depicts the experimental setup used for processing the glass substrates via LBF.

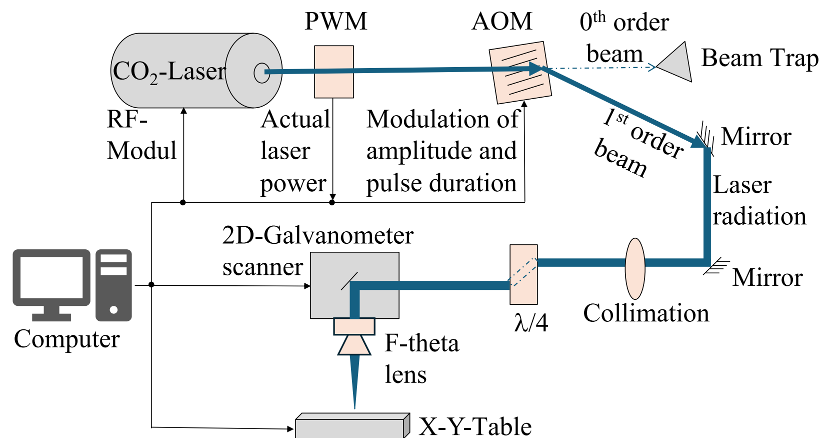

Fig. 1. Experimental setup for the processing of fused silica samples using LBF

The beam source utilized in this work is a power-stabilized CO_2 laser (Coherent, Inc., model Diamond CX-10L LCU) with a wavelength of $\lambda = 10.6\,\mu m$ [36]. A downstream pulse-width modulator (PWM) provides closed-loop control of the laser power, adjusting the output until a predefined setpoint is reached. An AOM is used to shape the beam into rectangular pulses. The beam is diffracted by the AOM's optical grating, and the first-order diffracted beam has a maximum amplitude efficiency of > 85%. The AOM can deflect a maximum laser power of 125 W at a frequency of 40.68 MHz and has a specified rise time of < 80 ns [37]. A 5th generation Real-Time Control card (Scanlab GmbH) is employed to control the amplitude and duration of the rectangular pulses [38]. This control card ensures the synchronous operation of the AOM and a 2D galvanometer scanner. Following the AOM, the modulated beam is collimated using a plano-convex zinc selenide lens. The initially linearly polarized radiation is then converted to circular polarization by a $\lambda/4$ phase retarder. The 2D galvanometer scanner deflects the circularly polarized pulses, and an f-theta lens focuses the deflected beam onto the sample surface. The used f-theta lens has a focal length of 200 mm. The sample is positioned underneath the scanner using a 3-axis stage system. The used LBF scanning strategy is shown in Fig. 2. A unidirectional scan

path with velocity v_{scan} moves the focused laser beam d_S across the sample surface. Individual laser pulses are separated by the pulse distance dx in the scan direction (intra-scan overlap). After completing one scan line, the beam path is displaced by the track distance dy perpendicular to the scan direction (inter-scan overlap). Continuous areal processing is achieved through overlapping pulses in both directions, with dx and dy controlling the degree of overlap and thus the local energy deposition and resulting surface modification depth.

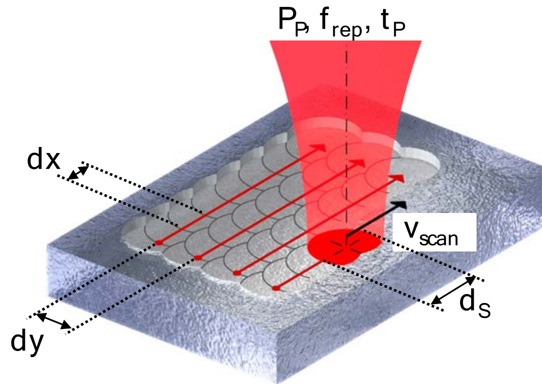

Fig. 2. Schematic of the LBF scanning strategy. The laser spot follows a unidirectional scan path with pulse distance dx (along track) and track distance dy (between successive scan lines).

The pulse duration range investigated in this work (20–52 μs) was selected based on previous studies [3,30] and thermal modeling considerations. According to the heat diffusion equation for CO_2 laser-glass interaction, the thermal penetration depth $L_{th} = 2\sqrt{(k \cdot t_W)}$, where k is the thermal diffusivity and t_W the interaction time, is approximately 2–5 μm for this parameter range. This ensures confinement of the thermally affected zone to the near-surface region while maintaining peak temperatures within the densification regime (1600–2200 °C) without excessive vaporization. The acousto-optic modulator's rise time of < 80 ns [37] enables precise temporal control, which is critical for achieving reproducible nanometer-scale removal depths.

To investigate deterministic material removal, flat fused silica samples are clamped into a custom sample holder. This holder allows for positioning the sample under the 2D galvanometer scanner with a repeatability of < 5 μm [30]. This level of precision is critical because the LBF process is site-selective. Any displacement of the sample during processing or upon re-positioning for subsequent correction passes would result in errors in the removal depth at the targeted surface locations. To ensure process reproducibility, all experiments were conducted under controlled laboratory conditions. Laser power stability was continuously monitored using the PWM feedback system, maintaining $P_L = 25$ W ± 0.5% throughout all experiments. Each parameter set was replicated on $N = 3$ spatially separated test fields to quantify inter-field variability.

2.2. White light interferometry

The achieved removal depths were measured using a White Light Interferometer (WLI) (Zygo, Nexview NX2). The instrument is equipped with four magnification objectives (1.4x, 5.5x, 20x, and 50x) and additional zoom lenses (0.5x, 1x, and 2x). The system's optical resolution is 520 nm, achieved with the 50x objective. Depending on the selected magnification, the sampling interval ranges from 0.09 μm/pixel to 12.38 μm/pixel, corresponding to a field of view between 0.09×0.09 mm^2 and 12.38×12.38 mm^2. The vertical resolution is specified as < 1 nm across all configurations [39]. Data analysis was performed using the manufacturer's proprietary software, MetroPro.

Continuous areal material removal in the LBF process is achieved by the spatial overlap of individual laser pulses in both the pulse and track directions. To characterize the process, a precise methodology was developed for evaluating the resulting surface topography. The ablation depth is defined as the mean height difference between the processed test surface and an immediately adjacent, unprocessed reference surface. This local referencing is critical to compensate for the influence of any global sample tilt, which can otherwise introduce significant errors when measuring removal depths on the nm scale. The investigation of process parameters was conducted on an 8×8 matrix of $2 \times 2\,\mathrm{mm}^2$ test fields. Each second field is processed resulting in a chessboard pattern. To ensure statistical robustness and quantify reproducibility, $N = 3$ identical test fields were processed for each parameter set. For the quantitative analysis, a $1 \times 1\ \mathrm{mm}^2$ square region of interest (ROI) was defined at the center of each test field (see Fig. 3). All reported depth values represent the mean of these $N = 3$ repetitions. This entire evaluation process was performed by a custom automated script to ensure objectivity. For the evaluation of areal process homogeneity over mm^2-scale regions, WLI provides both the required spatial sampling and sub-nm vertical resolution, whereas localized probe-based techniques (e.g., AFM) would undersample the characteristic process wavelengths (10–100 µm).

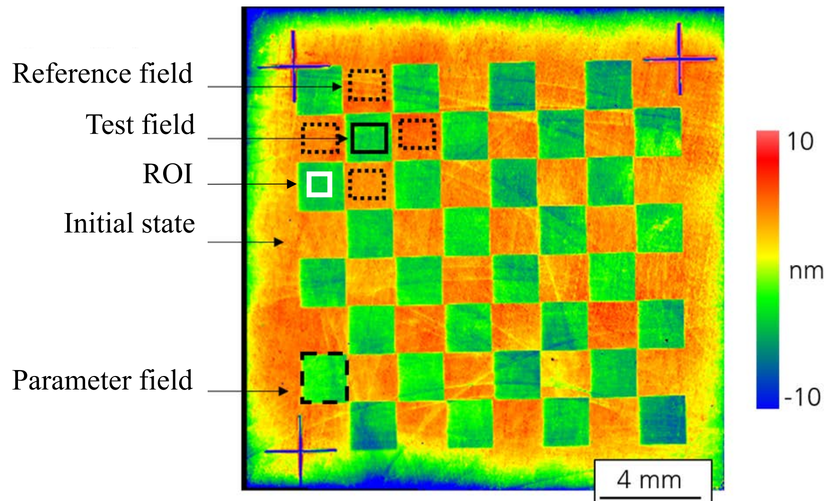

Fig. 3. WLI scan of a fused silica flat sample after processing by LBF, shown in false color (pre-annealing). The white square indicates the $1 \times 1\ \mathrm{mm}^2$ region of interest used for quantitative depth evaluation inside a test field.

2.3. Fused silica

The experiments described in this work were conducted on flat samples of fused silica (Corning 7980). Compared to other optical glasses, fused silica is exceptionally well-suited for laser-based thermal processing. Its high thermal resistance, characterized by a glass transition temperature of approximately 1585°C and a thermal shock resistance exceeding 2000 °C under atmospheric conditions, allows it to be processed without cracking. Furthermore, its high absorption coefficient of $\alpha > 80\%$ at the CO_2 laser wavelength of $\lambda = 10.6\,\mu\mathrm{m}$ makes it highly compatible with the beam source used. The material's low mean coefficient of thermal expansion, approximately $5.0 \cdot 10{-}7\,\mathrm{K}^{-1}$, is also critical. The LBF process is capable of inducing localized heating up to the vaporization temperature without causing crack formation in the surrounding material, a key advantage for high-precision surface modification [40]. For this study, two main categories of fused silica samples were investigated. The first category consisted of conventionally polished

substrates with an initial surface flatness of λ/20, available in two geometries: square plates of $20 \times 20 \times 10$ mm^3 and $80 \times 80 \times 3$ mm^3. The second category, utilized specifically for investigations on laser-based figure error correction, comprised 1-inch diameter, 5 mm thick fused silica discs. These discs were fabricated via laser polishing in a preceding step of a laser-based optics manufacturing process, with parameters detailed in [29]. It is known that the initial form accuracy of such laser-polished substrates varies significantly more than that of conventionally polished optics. A primary objective of these experiments was therefore to demonstrate that the LBF process can rapidly and cost-effectively improve the surface form of these substrates to meet standard specifications of the optics industry.

3. Results

3.1. Densification of areas

For LBF, the ability to induce precise and stable topographical changes is paramount. The primary metric for this process is the resulting surface ablation, which we define here as the processing depth, z_{ab}. A detailed discussion of the different interaction regimes for fused silica, which are critically dependent on the applied pulse duration, is provided in [3,4,30]. The authors delineate a progression of material modification: At specific parameters, material removal is inhibited, and the primary observed effect is localized densification. As the interaction parameters change, this transitions into a regime governed by exponential ablation characteristics, which is ultimately superseded by a third regime defined by linear material removal.

Each colored field in Fig. 4 represents a 2×2 mm^2 area processed with a specific pulse duration (20–40 µs), resulting in different densification depths (indicated by the false-color scale). The alternating pattern of processed and unprocessed fields enables differential height measurement using white light interferometry.

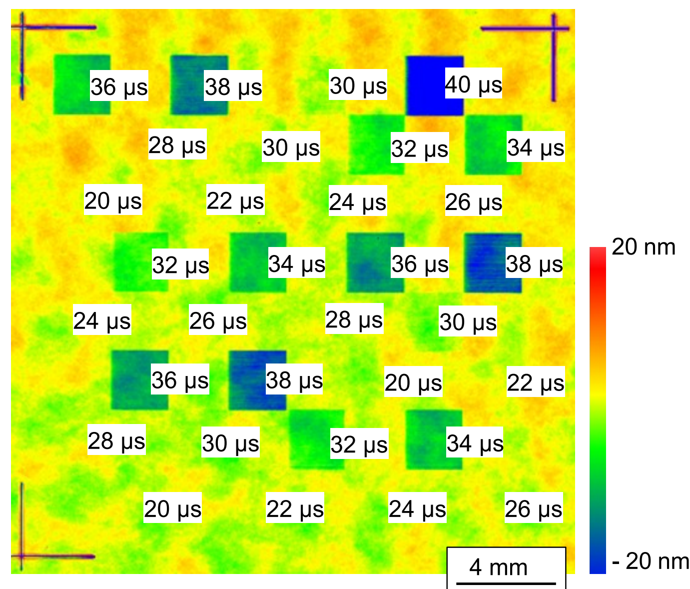

Fig. 4. False-color WLI image of a fused silica sample, showing densified areas generated by LBF with varying pulse durations to investigate their long-term stability. $P_L = 25$W, $f_{rep} = 1$ kHz, $dx = dy = 17.3$ µm and $d_S = 212$ µm.

To evaluate the long-term stability of this effect, a comprehensive experimental study was initiated. The investigation involved the creation of chessboard-patterned fields (see Fig. 4) on

Optics EXPRESS

fused silica samples, processed using a range of laser pulse durations that lead to densification. For statistical robustness, three identical test fields were generated and characterized for each distinct pulse duration. The topographical evolution of these fields was measured over an extended period using WLI, with measurements conducted at aperiodic intervals. The measurements for this long-term densification study were recorded in calendar week 3 of 2023 in Aachen, Germany.

The temporal evolution of the densification depth for four representative pulse durations is presented in Fig. 5, covering an observation period of 80 weeks. To assess the long-term stability of the induced densification, the surface depth z was monitored over an 80-week period. The experimental methodology was designed for statistical robustness and to distinguish process variability from measurement noise. At each time point, N = 3 distinct fields were processed and measured. Each final data point represents the average of 5 WLI acquisitions per field, which minimizes random instrument noise (specified uncertainty 1 nm, laboratory environment ± 1 K).

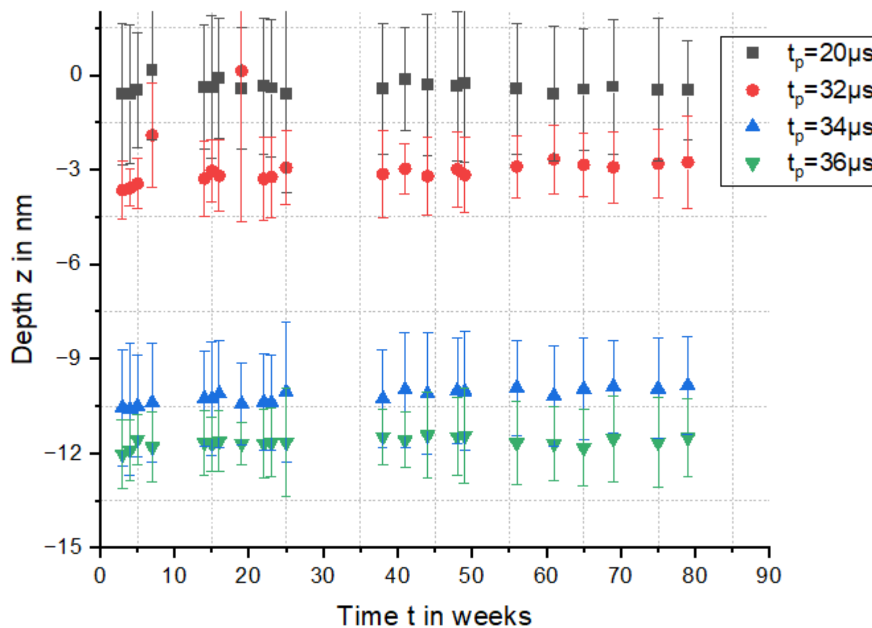

Fig. 5. Long-term stability of LBF-densified surfaces on fused silica: Mean densified depth plotted against time for a selection of different laser pulse durations. Error bars represent ± se (standard error of mean, N = 3 fields per time point). P_L = 25W, f_{rep} = 1 kHz, dx = dy = 17.3 μm, and d_S = 212 μm.

To validate this metric, a combined measurement uncertainty u_c was derived according to the GUM guidelines. The model accounts for the statistical spatial variability u_{stat}, the systematic instrumental resolution $u_{res} \approx 0.29$ nm, and thermal expansion effects u_{therm}. Due to the differential measurement principle relative to the substrate, u_{therm} was found to be negligible ($< 10^{-5}$ nm). Consequently, the total uncertainty is dominated by the process inhomogeneity ($u_c \approx u_{stat}$). This observation is empirically corroborated by the sub-threshold reference group ($t_p = 20$ μs). While the measured mean depth is physically negligible (-0.4 nm), the statistical uncertainty remains at $\bar{\sigma} \approx 2.1$ nm. This value effectively defines the detection limit of the experimental setup, imposed by surface roughness and spatial process variability.

Visual inspection of the time-series data in Fig. 5 suggests high stability, with no systematic drift or degradation visible over 80 weeks. To quantitatively assess whether any relaxation occurred, a Linear Mixed Model (LMM) was fitted to the quality-filtered dataset (N = 239

Optics EXPRESS

observations; RMS_{ref} quality threshold < 3 nm applied):

$$\text{densification depth} \sim \text{pulse duration} \times \text{calendar week} + (1\,|\text{Subfield})$$

Fixed effects comprised pulse duration, calendar week as a continuous time variable, and their interaction. A random intercept per Subfield (A, B, C, corresponding to lower, middle, and upper sample regions) explicitly modelled systematic spatial process inhomogeneity attributable to focus-position-dependent variations ($\sigma_{Subfield} = 1.352$ nm, $\sigma_{within} = 1.310$ nm, ICC = 0.516). The scatter visible in Fig. 5 is consistently explained by spatial process inhomogeneity between Subfield positions ($\sigma_{Subfield} = 1.352$ nm), attributable to focus-position-dependent variations, rather than by temporal relaxation, a distinction that the LMM captures explicitly through its random-effect structure. Model parameters were estimated by Restricted Maximum Likelihood (REML) and the p-values were obtained using Satterthwaite's method with Kenward-Roger degree-of-freedom correction (lme4/lmerTest, R). The results are summarized in Table 2.

Table 2. Statistical analysis of densification stability over 80 weeks (N = 239 observations after quality filtering). Linear Mixed Model (LMM) with Subfield as random effect ($\sigma_{Subfield} = 1.352$ nm, $\sigma_{within} = 1.310$ nm, ICC = 0.516). All LMM p-values use Kenward-Roger degree-of-freedom correction ($d_f \approx 229$).

Pulse duration in µs	LMM	
	Rate in nm/week (95% CI)	p-value
20	-0.0002 [−0.015, +0.015]	0.979
32	+0.0027 [−0.012, +0.018]	0.723
34	+0.0067 [−0.008, +0.021]	0.366
36	+0.0087 [−0.005, +0.023]	0.223

The LMM ANOVA (Type III) confirmed a significant effect of pulse duration on densification depth ($F(3,229) = 348.55$, $p < 0.001$), consistent with the established parametric dependence reported in [3,30]. Critically, neither the main effect of time ($F(1,229) = 1.451$, $p = 0.230$) nor the interaction between pulse duration and time ($F(3,229) = 0.292$, $p = 0.832$) reached statistical significance. Marginal relaxation rates estimated via *emtrends* in RStudio ranged from -0.0002 to +0.0087 nm/week across all pulse durations, with all 95% CI encompassing zero (Table 2). The $t_p = 20$ µs parameter showed no measurable rate ($p = 0.979$), as expected for this sub-threshold condition.

These results indicate that no statistically significant temporal relaxation of the densified surfaces is detectable over 80 weeks. All estimated rates are small in absolute magnitude (< 0.009 nm/week), he maximum point estimate corresponds to less than 0.7 nm over 80 weeks, within the detection limit of the experimental setup ($\bar{\sigma} \approx 2.1$ nm). The systematic spatial variability between Subfield positions accounts for approximately half of the total measurement variance and is explicitly modelled in the LMM rather than propagated as a source of error in regression slopes. Critically, visual inspection using optical microscopy confirmed no evidence of crack formation, delamination, or other modes of surface degradation on any processed area across the entire 80-week observation period.

For industrial applications, the key finding is that densified surfaces remain stable within the measurement uncertainty over at least 80 weeks for all investigated pulse durations. Given the current data, extrapolation of stability beyond the 80-week observation window is not statistically justified.

Optics EXPRESS

3.2. Ablation of areas

The optimal process parameters for areal material removal were determined through a systematic, two-phase experimental study. For all experiments, a unidirectional scanning strategy was employed with a fixed pulse-to-pulse distance of dx = 10 µm. The first phase involved a broad parameter screening, followed by a second phase that refined the process window using a smaller, statistically validated set of parameters. For both phases, parameter sets were processed in a randomized chessboard pattern to minimize thermal pre-heating effects. The results of the quantitative analysis are summarized in Fig. 6.

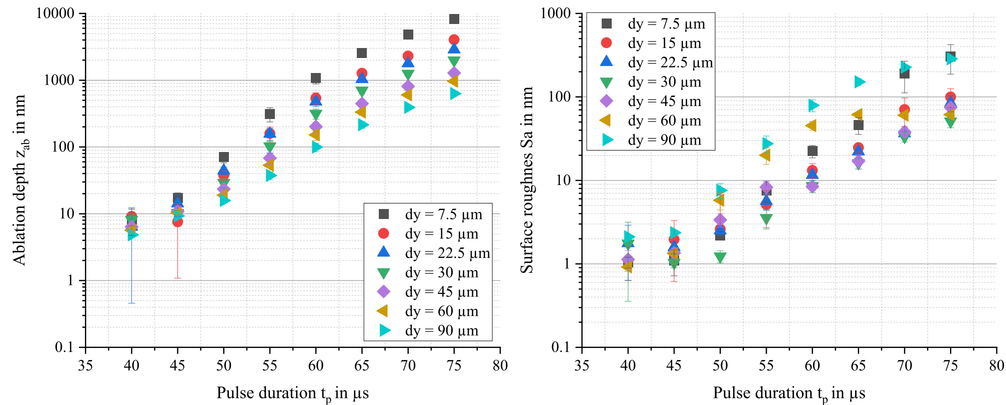

Fig. 6. Quantitative results of the parameter screening on areal laser ablation, showing ablation depth (left panel) and RMS surface roughness (right panel) as a function of pulse duration for various track distances dy. All experiments were conducted with a single pass using $P_L = 25$ W, dx = 10 µm and $d_S = 326$ µm.

Based on the initial screening, the fundamental process characteristics were identified, showing that the ablation depth increases with the pulse duration t_p and decreases with track distance. This study identified that very large track distances (dy ≥ 60 µm) result in poor surface quality due to insufficient track overlap, while the smallest track distance (dy = 7.5 µm) also produced higher roughness at increased pulse durations. The refined study (Fig. 7) provided a more detailed view, confirming these trends and clearly showing a transition from a material densification-dominated regime ($z_{ab} < 10$ nm for $t_p \leq 47$ µs) to a true ablation regime, marked by a disproportionate increase in both removal depth and surface roughness for $t_p \geq 50$ µs. Throughout both studies, a track distance of dy = 30 µm consistently yielded a favourable combination of controlled removal and low surface roughness. To investigate the crucial trade-off between process efficiency and final surface quality, a detailed topographical analysis was performed. Figure 7 present direct comparisons of surfaces processed to nearly identical ablation depths using different parameter sets.

The first comparison Fig. 7, (1) and (2), for a target depth of ∼ 26 nm, shows that using a larger track distance dy = 30 µm results in a significantly smoother surface of 1.3 nm RMS compared to a smaller track distance dy = 7.5 µm, with 2.3 nm RMS, as evidenced by the more uniform texture and reduced PV variations visible in the topography map while simultaneously reducing the processing time by a factor of four. This finding is reinforced by the second comparison Fig. 7, (3) and (4), for a greater target depth of ∼ 45 nm. Here again, dy = 30 µm produced a superior surface finish with 2.1 nm vs. 2.8 nm RMS and halved the processing time compared to using dy = 15 µm. In conclusion, these investigations consistently demonstrate that employing a larger track distance, when appropriately paired with pulse duration, not only enhances process efficiency but also produces a superior surface finish for a given ablation depth. Based on these

Optics EXPRESS

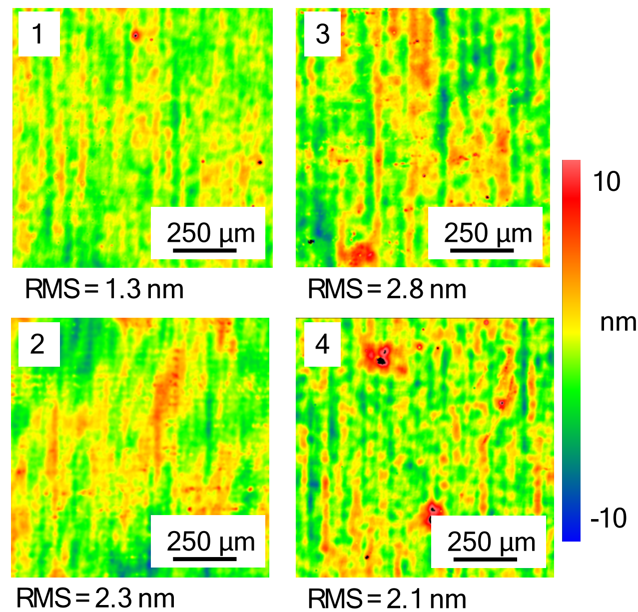

Fig. 7. WLI topography maps comparing LBF strategies for two target ablation depths. Panels (1) and (2): ~26 nm depth using dy = 30 µm, t_p = 50 µs vs. dy = 7.5 µm, t_p = 47 µs (RMS = 1.3 nm vs. 2.3 nm). Panels (3) and (4): ~45 nm depth using dy = 15 µm, t_p = 50 µs vs. dy = 30 µm, t_p = 52 µs (RMS = 2.8 nm vs. 2.1 nm). All processes: single pass, P_L = 25 W, dx = 10 µm, d_S = 326 µm.

comprehensive results, the optimal parameters for this LBF process were determined to be a pulse distance of dx = 10 µm and a track distance of dy = 30 µm.

The observed transition for t_p between 47 µs and 50 µs corresponds to a shift in the dominant material removal mechanism. For $t_p \leq 47$ µs, the induced surface depression results primarily from glass network densification. A rapid cooling from the melt/softening temperature (1600–2000 °C) freezes a higher-density structural configuration, manifesting as a topographical depression without mass loss. This mechanism is supported by the reversibility of the effect upon thermal annealing [3]. At $t_p \geq 50$ µs, the increased energy input raises the surface temperature above the vaporization threshold, initiating material evaporation. This transition is evidenced by the disproportionate increase in removal depth from less than 10 nm to 45 nm despite modest pulse duration change, concurrent roughness increase from 1.3 nm to 2.5 nm RMS indicating non-uniform evaporation fronts, and visible changes in processed surface morphology under optical microscopy. The intermediate regime at t_p = 47–50 µs exhibits mixed characteristics, with both densification and incipient ablation contributing to the net removal.

The identified optimal spatial parameters (dx = 10 µm, dy = 30 µm) correspond to pulse and track overlaps of 97% and 91%, respectively, relative to the laser spot diameter d_S = 326 µm. This high degree of overlap is necessary to ensure continuous densification/ ablation across the processed area while avoiding excessive thermal accumulation. The larger track distance ($dy/d_S \approx 0.09$) compared to the pulse distance ($dx/d_S \approx 0.03$) reflects the unidirectional scanning strategy. Thermal pre-heating along the scan direction enables tighter pulse spacing, whereas inter-track thermal gradients necessitate wider track separation to prevent cumulative heating effects that would otherwise increase surface roughness.

3.3. Figure error correction using LBF

This section investigates the figure error correction of a ground and subsequently laser polished fused silica substrate using LBF. The initial ground and laser polished surface, characterized over an $8 \times 8\,\text{mm}^2$ area, exhibited significant form deviation and high roughness, with an unfiltered RMS value of 79.2 nm. The objective is to reduce the substantial initial form error, on the order of several hundred nanometers PV across the evaluation area, by applying a single LBF corrective pass (see Fig. 8).

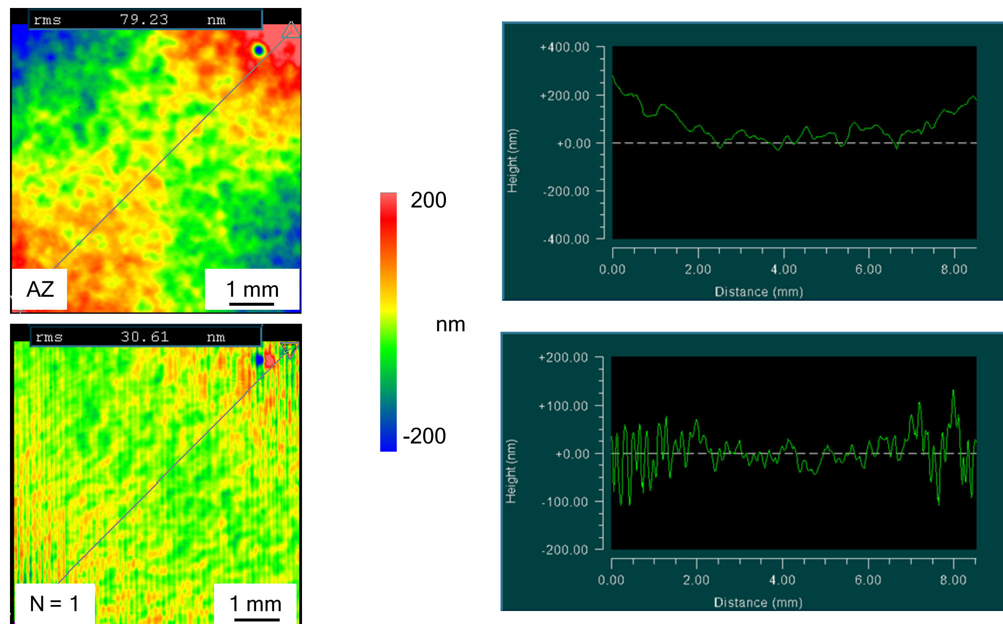

Fig. 8. WLI false-color topography maps of a laser-polished surface before (top, AZ) and after (bottom, N = 1) LBF correction, shown over an $8 \times 8\,\text{mm}^2$ area. The color scale represents height deviations from a fitted reference plane. Initial RMS = 79.2 nm; corrected RMS = 30.6 nm Process parameters: $P_L = 25$ W, $dx = 10\,\mu\text{m}$, $dy = 30\,\mu\text{m}$, $d_S = 326\,\mu\text{m}$.

The subsequent analysis confirmed a successful figure error correction, as the unfiltered surface RMS value was significantly reduced from 79.2 nm to 30.6 nm. WLI measurements taken after the procedure verified the effectiveness of the correction, particularly at the edges of the processed area. However, the results revealed a key process trade-off: while LBF effectively corrected low- and mid-frequency form errors, it concurrently introduced high-frequency roughness at spatial wavelengths below 100 µm. To mitigate this induced micro-roughness, a final finishing step is deemed necessary. It is proposed that a conventional chemo-mechanical process, such as traditional pitch polishing, could effectively smooth the surface. While this technique is well-established in industrial optics manufacturing, the verification of its application following an LBF correction remains a subject for future investigation.

4. Discussion and conclusion

Laser Beam Figuring (LBF) on fused silica induces deterministic, non-ablative topography changes via localized densification. This mechanism is consistent with a fictive-temperature modification resulting from rapid quenching and is supported by the process's reversibility upon thermal annealing, which rules out ablation as the dominant mechanism. Regarding potential optical property changes, prior investigations by Weingarten [3] included refractive

Optics EXPRESS

index measurements on LBF-processed fused silica. These measurements detected no significant change in refractive index within the measurement uncertainty (4th decimal place). Additionally, stress birefringence measurements confirmed values < 5 nm/cm, which are within specifications for mirror applications. While the thermal penetration depth for LBF is comparable to the measurement depth, these results suggest that refractive index perturbations, if present, are below the detection threshold for the investigated process parameters. A more detailed spectroscopic and spatial characterization (e.g., Raman spectroscopy to probe structural changes in the glass network, or high-resolution ellipsometry) would provide further insight into the fictive temperature distribution and its correlation with densification depth but was beyond the scope of this study.

The 80-week stability study confirmed the absence of any statistically significant temporal relaxation across all investigated pulse durations, with all estimated rates lying well within the experimental detection limit (Table 2). The scatter visible in Fig. 5 is consistently explained by spatial process inhomogeneity between Subfield positions ($\sigma_{\mathrm{Subfield}} = 1.352$ nm), attributable to focus-position-dependent variations, rather than by temporal relaxation, a distinction that the LMM captures explicitly through its random-effect structure. No crack formation or delamination was observed throughout the observation period. For mirror figuring applications, the point estimate of any potential relaxation does not exceed 0.7 nm over 80 weeks across all investigated pulse durations, well within the tolerance requirements for the intended application. It is worth noting that at this signal-to-noise ratio, the absence of statistical significance cannot be equated with absolute stability over arbitrarily long timescales, rather, it establishes that any potential relaxation is bounded by the detection limit of the experimental setup ($\bar{\sigma} \approx 2.1$ nm).

For ultra-precision applications requiring sub-nm form stability over multi-year timescales, three complementary strategies merit further investigation: extended monitoring beyond two years with improved metrological protocols, accelerated aging studies at elevated temperatures, and the integration of LBF as a near-final step prior to ultra-low-removal-rate finishing such as IBF or pitch polishing. Whether very slow relaxation processes may operate over multi-year timescales, potentially facilitated by ambient humidity (laboratory conditions: 40 - 60% RH), cannot be excluded based on the present data. Controlled-environment studies over periods exceeding two years would be required to investigate this question. Table 3 positions LBF within the landscape of deterministic figuring technologies.

Compared to IBF, LBF offers higher area rates (0.11 cm^2/s vs. 0.01 - 0.1 cm^2/s), while achieving competitive throughput with MRF (0.1 - 0.5 cm^2/s). Compared to both technologies, LBF offers lower capital/operational costs, making it particularly attractive for rapid prototyping and medium-volume production for fused silica optics. However, the achievable RMS surface quality (2–30 nm) and limited spatial frequency correction range ($\lambda > 100\,\mu$m) position it as a complementary technology rather than a direct replacement. For ultra-precision applications requiring sub-nm roughness (e.g., EUV optics), IBF remains indispensable. For mid-spatial-frequency corrections ($\lambda = 3$–10 mm), MRF is superior. LBF's unique advantage lies in its integration capability within laser-based manufacturing chains (ablation → polishing → LBF) without workpiece transfer or tool changes, combined with quantified long-term stability. Compared to femtosecond laser approaches, CO_2-based LBF provides cost advantages (factor 10–20 in laser source) and larger effective processing areas, though at the expense of lateral resolution. The optimal industrial strategy may involve hybrid process chains combining these technologies based on component specifications.

An instructive comparison can be made with Han et al. [41], who developed a fundamentally different CO_2-based approach. Their "densi-melting effect" operates in the densification-melt regime ($T < 2200$ K) without evaporation, an "equal material" mechanism where form correction arises from volumetric shrinkage (3–25 nm) rather than mass removal. The clustered overlapping technology treats $3 \times 3\,mm^2$ sub-regions as discrete tool influence functions, mechanically eliminating scanning ripples and achieving full-spatial-frequency convergence with sub-0.3 nm

Table 3. Comparative analysis of deterministic surface figuring technologies for fused silica optics.

Technology	Removal mechanism	Depth range / area rate	Surface quality (RMS)	Long-term stability	Key advantages vs. limitations
MRF	Chemo-mechanical	10-1000 nm / 0.1-0.5 cm^2/s	0.3-2 nm	Demonstrated	Mature, sub-nm roughness vs contamination risk
IBF	Sputtering	1-100 nm / 0.01-0.1 cm^2/s	<0.2 nm	Demonstrated	Ultra-precision vs. very slow, expensive
fs-Laser (Otieno 2025) [35]	Photochemi-cal + thermal	Local smoothing / µm-scale	Sub-nm (local)	Not demonstrated	High lateral resolution vs. small area, no form correction
CO_2, LBF (Han 2023) [41]	Densi-melting (equal material)	3-25 nm / ~0.0015 cm^2/s	0.27-0.45 nm	Not investigated	Ultra-low roughness, MSF suppression vs. very slow (4.5 h/25mm^2), small area
CO_2, LBF (This work)	Densification + Ablation	0.7-45 nm / ~0.11 cm^2/s	1.3-30.6 nm	80 weeks, no significant relaxation detected	Fast, large area, quantified stability vs. high-freq. texture (post-polish required)

roughness. Our approach includes the ablation regime (T > 2200 K), enabling larger removal depths (0.7–45 nm) and significantly higher throughput (estimated 0.11 cm^2/s vs. 0.0015 cm^2/s, approximately 73x faster). While Han's method achieves superior spatial frequency control, it is limited to smaller areas (5×5 mm^2, 4.5 hours processing). Our approach prioritizes scalability (16×16 mm^2, 240 s) and provides quantified long-term stability (80-week study, not investigated in Han's work), but introduces high-frequency texture ($\lambda < 100$ µm) requiring post-polishing. These complementary CO_2 variants should be selected based on specifications: Han's approach for ultra-smooth, small-aperture components; ours for rapid prototyping where post-polishing is acceptable.

The process mapping results (Section 3.2) provide quantitative guidelines for parameter selection. The observed transition from densification-dominated behavior ($t_p \leq 47$ µs, $z_{ab} <$ 10 nm) to the ablation regime ($t_p \geq 50$ µs) correlates with exceeding the vaporization threshold of SiO_2. In the densification regime, material removal results primarily from volume densification, whereas ablation involves actual mass loss via vaporization. The concurrent increase in surface roughness at $t_p \geq 50$ µs (from 1.3 nm to > 2.5 nm RMS) indicates the onset of non-uniform evaporation and possible melt flow instabilities. The identified optimal parameters, in these studies, balance these competing mechanisms, achieving removal depths up to 45 nm while maintaining RMS < 2.1 nm. The figure error correction demonstration (Section 3.3) validates the process for real-world applications but also reveals a fundamental trade-off. While LBF effectively corrects low-to-mid spatial frequency errors, it introduces high-frequency texture at $\lambda < 100$ µm. This behavior is inherent to the discrete pulse-overlap strategy and the finite spot size. For mirror applications in non-critical wavelength regimes, this micro-texture may be acceptable. For demanding applications (e.g., laser optics, imaging systems), a final chemo-mechanical polishing step using conventional pitch or sub-aperture tools is recommended to remove the high-frequency component without affecting the corrected form. The compatibility of LBF-processed surfaces with subsequent pitch polishing has been qualitatively confirmed in preliminary tests but requires systematic characterization in future work.

Funding. German Federal Ministry for Economic Affairs and Energy (BMWE).

Optics EXPRESS

Acknowledgment. This research was funded by the German Federal Ministry for Economic Affairs and Energy (BMWE) within the Promotion of Joint Industrial Research Programme (IGF) due to a decision of the German Bundestag. It was part of the research project [21672 N] by the Association for Research in Precision Mechanics, Optics and Medical Technology (F.O.M.) under the auspices of the DLR Projektträger (DLR-PT).

Disclosures. The authors declare that there are no financial interests, commercial affiliations, or other potential conflicts of interest that could have influenced the objectivity of this research or the writing of this paper.

Data availability. Data underlying the results presented in this paper are not publicly available at this time but may be obtained from the authors upon reasonable request.

References

1. L. F. Wang, Y. W. Hu, and Z. G. Zhang, "Rapid manufacturing technology for aspheric optical elements," Opto-Electron Eng. **51**, 230171 (2024).
2. S. Heidrich, Abtragprozesse und Prozesskette zur laserbasierten Fertigung optischer Elemente aus Quarzglas, RWTH Aachen Dissertation. Aachen2014.
3. C. Weingarten, Laserbasierte Formkorrektur von optischen Gläsern, RWTH Aachen University Dissertation. Aachen2017.
4. A. Temmler, C. B. Weingarten, B. Schober, *et al.*, "Investigation on laser beam figuring of fused silica using microsecond pulsed CO2 laser," Appl. Surf. Sci. **555**, 149609 (2021).
5. A. H. Fritz and G. Schulze, *Fertigungstechnik, Bd. 0* (Springer Berlin Heidelberg: Berlin, Heidelberg, 2010).
6. G. Litfin, *Technische Optik in der Praxis* (Springer: Berlin, Heidelberg, New York, 2001).
7. G. Fales and M. Weinacht, *Asphärische Linsen: Korrektur der chromatischen Aberration* (Optik: Spezial, 2010).
8. S. Nollau, M. Wellensiek, and D. Hollstegge, *Designempfehlungen für das Präzisionsblankpressen* (Photonik2010).
9. A. T. Beaucamp, Y. Namba, and R. Freeman, "Development of hybrid fluid jetfloat polishing process," Proc. of SPIE **8838**, 88380P (2013).
10. T. Sun, L. Sun, Y. Jin, *et al.*, "Research on the fluid jet polishing in advanced optical fabrication," *7th International Symposium on Advanced Optical Manufacturing and Testing Technologies (AOMATT 2014)*. SPIE Proceedings. SPIE2014, 92812Q
11. F. Kazemi, G. Boehm, and T. Arnold, "Optical freeform generation of N-BK7 by fluorine-based plasma jet machining," Proc. of SPIE **11478**, 1147805 (2020).
12. T. Arnold, G. Boehm, I.-M. Eichentopf, *et al.*, "Plasma Jet Machining. A novel technology for precision machining of optical elements," Vak. Forsch. Prax. **22**(4), 10–16 (2010).
13. P. K. Baghel, V. Mishra, R. Kumar, *et al.*, "Ultrasonic vibration–assisted magnetorheological hybrid finishing process for glass optics," The International Journal of Advanced Manufacturing Technology **125**(5-6), 2265–2276 (2023).
14. K. F. Beckstette, "Ultrapräzise Oberflächenbearbeitung am Beispiel von Lithografieoptiken," Ultraprecise Surface Figuring for Lithography Optics. tm - Technisches Messen **69**, 526 (2002).
15. M. Chen, H. Liu, J. Cheng, *et al.*, "Model of the material removal function and an experimental study on a magnetorheological finishing process using a small ball-end permanent-magnet polishing head," Appl. Opt. **19**, 5573–5582 (2017).
16. D. D. Walker, D. Brooks, A. King, *et al.*, "The 'Precessions' tooling for polishing and figuring flat, spherical and aspheric surfaces," Opt. Express **11**(8), 958–964 (2003).
17. S. R. Wilson and J. R. McNeil, "Neutral Ion Beam Figuring Of Large Optical Surfaces," Curren Developments in Optical Engineering II **818**, 320 (1987).
18. M. Weiser, "Ion beam figuring for lithography optics," Elsevier **267**, 1390–1393 (2009).
19. M. Zeuner and S. Kiontke, "Ion Beam Figuring Technology in Optics Manufacturing," Opt. Photonik **7**(2), 56–58 (2012).
20. K. M. Nowak, "Rapid Prototyping of Micro-Optics for Brightness Restoration of Diode Lasers," Dissertation. Edinburgh: Heriot-Watt University 2003.
21. K. M. Nowak, H. J. Baker, and D. R. Hall, "Pulsed laser machining and polishing of silica micro-optical components using a CO2 laser and an acousto-optic modulator," Photonics Fabrication Europe **4941**, 468512 (2002).
22. K. Hecht, *Entwicklung eines Laserstrahl-polierverfahrens für Quarzglasoberflächen* (Universitätsbibliothek: Ilmenau, 2012).
23. A. Richmann, Polieren von Gläsern und Kunststoffen mit CO2-Laserstrahlung. Zugl.: Aachen, Techn. Hochsch., Diss., 2013. Berichte aus der Lasertechnik. Aachen: Shaker 2013.
24. P. A. Temple, W. H. Lowdermilk, and D. Milam, "Carbon dioxide laser polishing of fused silica surfaces for increased laser-damage resistance at 1064 nm," Appl. Opt. **21**(18), 3249–3255 (1982).
25. K. Hecht, J. Bliedtner, M. Rost, *et al.*, "Carbon-Dioxide Laser Beam Polishing of Fused Silica Surfaces - Process Development and Optimization," Adv. Eng. Mater. **17**(3), 240–246 (2015).
26. S. Heidrich, E. Willenborg, and A. Richmann, "Development of a Laser Based Process Chain for Manufacturing Freeform Optics," Phys. Procedia **12**, 519–528 (2011).
27. S. Kim, J. Kim, Y.-H. Joung, *et al.*, "Optimization of selective laser-induced etching (SLE) for fabrication of 3D glass microfluidic device with multi-layer micro channels," Micro and Nano Syst. Lett. **7**(1), 15 (2019).

Optics EXPRESS

28. J. Qi, Z. Wang, J. Xu, *et al.*, "Femtosecond laser induced selective etching in fused silica: optimization of the inscription conditions with a high-repetition-rate laser source," Opt. Express **26**(23), 29669–29678 (2018).
29. M. Jung, Einfluss des Temperatur-Zeit-Verlaufs auf Formtreue und Welligkeit bei der Laserpolitur von Glas, RWTH Aachen University Dissertation. Aachen 2025.
30. E. Uluz, Untersuchungen zur Prozessstabilität beim Laser Beam Figuring von Quarzglasoberflächen, RWTH Aachen University Masterarbeit. Aachen 2022.
31. K. L. Wlodarczyk, *Surface deformation mechanisms in laser smoothing and micromachining of optical glasses* (Heriot-Watt University2011).
32. L. Robin, P. Combis, P. Cormont, *et al.*, "Infrared thermometry and interferential microscopy for analysis of crater formation at the surface of fused silica under CO2 laser irradiation," J. Appl. Phys. **111**(6), 6 (2012).
33. S. Elhadj, M. J. Matthews, S. T. Yang, *et al.*, "Evaporation kinetics of laser heated silica in reactive and inert gases based on near-equilibrium dynamics," Opt. Express **20**(2), 1575–1584 (2012).
34. S. Heidrich, A. Richmann, P. Schmitz, *et al.*, "Optics manufacturing by laser radiation," Optics and Lasers in Engineering **59**, 34–40 (2014).
35. C. Otieno and J. Qiao, "Femtosecond laser figuring and polishing of fused silica with GHz-burst mode [Invited]," Opt. Mater. Express **15**(7), 1510–1519 (2025).
36. Coherent Inc., Diamond Cx-10 Series, 2024. https://www.coherent.com/content/dam/coherent/site/en/resources/datasheet/lasers/COHR_DiamondCx-10_DS_1120_1.pdf, online checked: 11.04.2024.
37. Gooch and Housego UK: Ge AOM – SINGLE FREQUENCY. Ge Acousto-Optic Modulator for High-Power, 9.4 or 10.6 µm Applications, 2017. https://gandh.com/products/acousto-optics/modulators/i-m041-xxc11xxx-p5-gh77, online checked: 27.01.2024.
38. SCANLAB GmbH: RTC5. Ansteuerkarten. https://www.scanlab.de/de/produkte/steuerungselektronik/rtc-ansteuerkarten, online checked: 11.04.2024.
39. Zygo Corporation: ZYGO Nexview2 Specifications, 2022. https://www.zygo.de/products/metrology-systems/3d-optical-profilers/nexview-nx2, online checked: 11.04.2024.
40. Corning: HPFS Product Brochure All Grades 2015_07_21, 2024. https://www.corning.com/media/worldwide/csm/documents/HPFS_Product_Brochure_All_Grades_2015_07_21.pdf.
41. Y. Han, S. Wan, X. Peng, *et al.*, "Densi-melting effect for ultra-precision laser beam figuring with clustered overlapping technology at full-spatial-frequency," Opt. Express **31**(11), 17364–17379 (2023).